ACS APPLIED NANO MATERIALS

www.acsanm.org Article

Nanowell-Based Orthogonal Submicropolarizer Array Biochip for Multiple Throughput of Fluorescence Sequencing

Hsin-Yi Hsieh,* Chung-Hao Lin, Wei-Ko Wang, and Chin-Chuan Hsieh

Cite This: *ACS Appl. Nano Mater.* 2021, 4, 10409−10418 Read Online

ACCESS | Metrics & More | Article Recommendations | Supporting Information

ABSTRACT: Overcoming the diffraction limit is a great challenge to increasing the nanowell density. A methodology differing from super-resolution microscopy is introduced to realize a theoretical $\sqrt{2}$- or $\sqrt{3}$-fold resolution improvement *via* two-step imaging and simple equipment adaptations: (1) a biochip integrated with an orthogonal-orientation nano/micropolarizer array in an interspaced arrangement with reaction sites and (2) an optical system inserted with an angle-switchable polarizer plate to generate polarized light for illumination. Because the 0° polarized light will be blocked by the 90° polarizer units, only half of the signals on the polarizer array with the same polarization angle can be acquired, and a virtual distance occurs between any two "bright" fluorescence signals. We have demonstrated that a 0.9 μm pitch wide-field image unresolvable *via* a 20×/NA0.5 objective can be divided into two resolvable images with an 8−10 signal-to-noise ratio (SNR) based on this approach. The aluminum polarizer array on the biochip had a 180 nm thickness, 0.9 μm pixel size, 300 nm period, and ∼0.55 fill factor. This method could be used for practical fluorescence-based nanoarray analysis, such as next-generation sequencing (NGS), to either enlarge the field of view to accelerate the scanning speed of a whole chip or increase the reaction density for multiple throughputs, and thus the sequencing cost can be reduced.

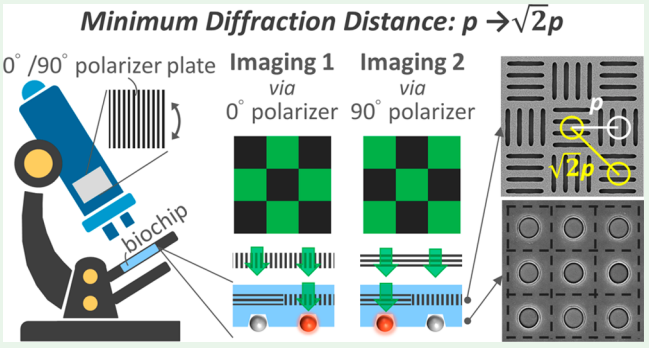

KEYWORDS: *biochip, nanoarray, micropolarizer array (MPA), diffraction limit, super-resolution microscopy, fluorescence sequencing*

INTRODUCTION

Periodically patterned micro/nanoarray technologies, including general photolithography,[1] microcontact printing,[2,3] nanoimprinting,[4] interferometry lithography,[5,6] nanosphere lithography,[7,8] and metal-assisted chemical etching (MacEtch),[9,10] have served as an essential platform to realize cost-effective *in vitro* diagnostics.[1,11−14] One popular tactic to report biomedical reactions relies on the presence of fluorescence signals, such as in microarrays for multiplexed infectious disease identification[13,15] and nanoarrays for DNA sequencing.[14,16] In particular, next-generation sequencing (NGS), in which a sequence-by-synthesis procedure is performed to decode the clonal DNA cluster in each spot, which is reassembled into a genome, has exploited the massively parallel analysis capability of a patterned array in the extreme.[14,17−19] However, the array pitch size of a flow cell has recently remained at 600−900 nm without a great reduction due to the spatial resolution limit of the optical detection system.[20]

The diffraction barrier of a conventional optical microscope restricts the minimum distance to distinguish two objects.[21,22] The Rayleigh criterion specifies that the minimum resolvable separation between two light beams is $0.61\lambda/NA_{obj}$, where the first minimum of the one point spread function (PSF) coincides with the maximum of the other PSF.[22] Thus, the diffraction barrier of the microscope resolution is approximately 250 nm in the lateral direction when an oil-immersion objective with a numerical aperture (NA) of 1.50 is used.[23] Under imperfect conditions, the resolution may be lower still.[24] However, the optical system of leading NGS sequencers adopts an air objective with a long working distance (WD) and a low magnification for rapid scanning capture of images of the flow cell containing two or four fluorescent dyes covering wavelengths of 550−740 nm. For example, the Illumina HiSeq 2000 utilizes a 20×/NA0.75 Nikon objective with a 1 mm WD, which results in a Rayleigh resolution of ∼602 nm and restricts the minimum well pitch of the above-mentioned flow cell. Although the resolution can be improved by using an objective with a higher NA, the field of view and the WD will be noticeably reduced, which raises difficulties in scanning image capture and reassembly for a flow cell.

Received: July 13, 2021
Accepted: September 27, 2021
Published: October 6, 2021

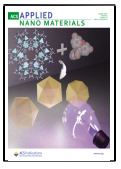

https://doi.org/10.1021/acsanm.1c01936
ACS Appl. Nano Mater. 2021, 4, 10409−10418

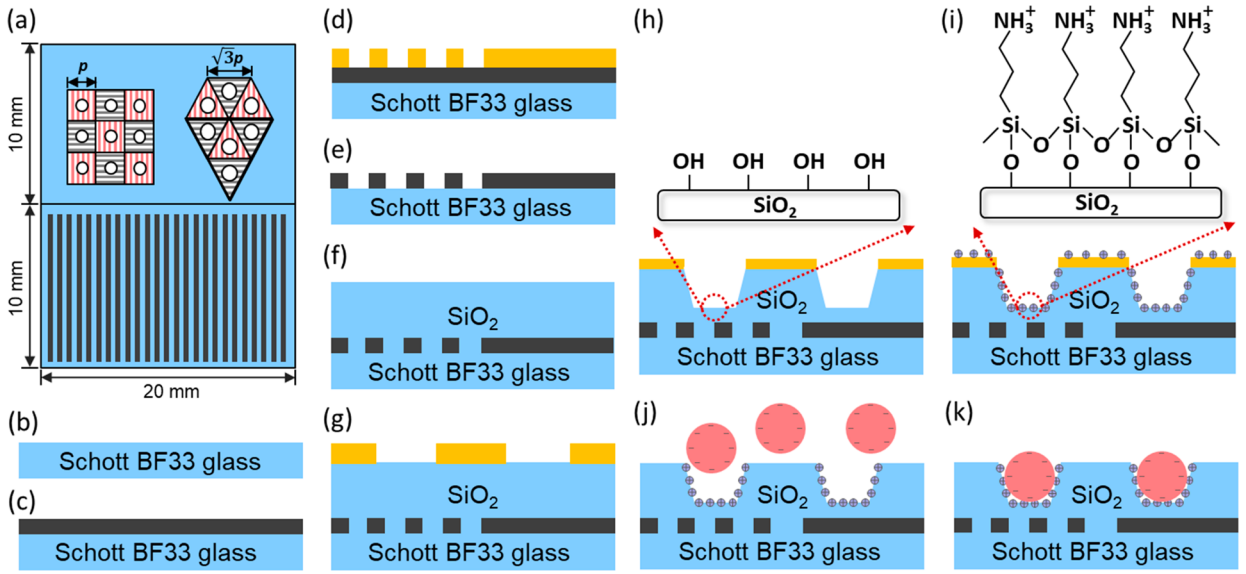

Figure 1. Schematic illustration of the chip layout and fabrication process, as well as the fluorescent bead loading process. (a) The chip layout is equally divided into two parts: the upper half includes square and triangular nano/micropolarizer arrays with pitch sizes, p, of 0.6, 0.9, 1.2, 1.5, 3, and 6 μm and the bottom half includes a large polarizer plate. The fabrication process of the upper half includes (b) oxygen plasma treatment on an 8 in. BF33 glass, (c) deposition of an Al layer on the glass, (d) PR definition of the grating pattern by 248 nm DUV lithography, (e) dry etching through the Al layer to form a nano/micropolarizer grating array, (f) 700 nm SiO_2 deposition on the substrate, (g) PR definition of the nanowells by 248 nm DUV lithography, and (h) dry etching of SiO_2 to form nanowells on the nano/micropolarizer array. The fluorescent bead loading process includes (i) APTES modification of the nanowell surface with amine groups, (j) immersion of the chip in a liquid solution with negatively charged fluorescent beads, and (k) washing and air drying to remove excess beads for one bead in a nanowell loading.

Numerous super-resolution microscopy technologies, such as structured illumination microscopy (SIM), photoactivated localization microscopy (PALM), stochastic optical reconstruction microscopy (STORM), and stimulated emission depletion (STED) microscopy, have been developed to reduce the diffraction barrier from ~250 to ~10 nm.[21,23,25] SIM employs illumination of the sample through a known spatially structured pattern (e.g., a grating nanostructure) to generate sinusoidal interference patterns in the images, and multiple images captured *via* movement and/or rotation of the grating nanostructure in one or more dimensions are mathematically deconvoluted. The other techniques rely on spatial or temporal modulation of the transition between two photoswitching states of a fluorescent molecule, such as in PALM and STORM, or on optically reducing the effective size of the PSF used in the excitation illumination, such as in STED.[21,23] Among them, the SIM family is more popular due to its simple optics, rapid imaging speed, 10^3–10^6 lower illumination intensities, and high compatibility with any kind of fluorophore. Although the 2 times resolution improvement needs a Fourier deconvolution procedure, it can still generate a $\sqrt{2}$ improvement in resolution in a single camera exposure.[26,27]

Interestingly, illumination *via* a grating nanostructure has also been employed in fields including optical communications, displays, and imaging systems. For example, visualization through a grating polarizer or pixelated polarizer array provides the orientation direction information on the reflected plane of an object,[28,29] eliminates reflections and glare on smooth surfaces,[30,31] enhances the contrast of scratches and stains,[32] and helps in analyzing the distortion due to mechanical stress in transparent objects.[3033] Additionally, when incorporated with various optical stacks and arrangements, the grating polarizer has realized a dual-view three-dimensional display from one display panel[34,35] and a snapshot multispectral camera.[36,37] Apart from the pure polarization property at visible light wavelengths with a grating period of smaller than 200 nm, wire grid grating nanostructures have been reported in applications for their additional wavelength selection capability that varies with the grating period, incident angle, and nanostructure materials, including a single metal layer made of silver (Ag), gold (Au), or aluminum (Al) and a sandwich stack of dielectrics and metals.[28,38−42]

In this paper, we exploit the polarization and long-pass filter properties of Al grating nanostructures to generate 0 or 90° polarized light that exposes the nanowells through the embedded Al nano/micropolarizer array with two orthogonally oriented polarization angles for interval illumination in the space of nanowells to generate a virtual distance (dark spacing) among neighboring reaction sites (any two bright signals).[43] By considering an appropriate interspaced arrangement in a square or triangle shape, we demonstrated super-resolution imaging in another form to break the diffraction limit with a theoretical $\sqrt{2}$- or $\sqrt{3}$-fold improvement by a two-step imaging capture method.

RESULTS AND DISCUSSION

Nanowell-Based Orthogonal Submicropolarizer Array Biochip. The nanowell chip was designed and placed on an interspaced Al nano/micropolarizer array with two orthogonally oriented polarization angles in a square or triangular arrangement (Figure 1a–h). The pitch sizes, p, of the nanowells include 0.6, 0.9, 1.2, 1.5, 3, and 6 μm for 2, 3, 4, 5, 10, and 20 pairs of 300 nm grating period in one square nano/micropolarizer unit. To imitate the fluorescence response at the reaction sites, SiO_2 nanowells were fabricated in a diameter of ~450 nm and a depth of 350 nm, and 400 nm fluorescent beads were immobilized in them to realize the

https://doi.org/10.1021/acsanm.1c01936
ACS Appl. Nano Mater. 2021, 4, 10409−10418

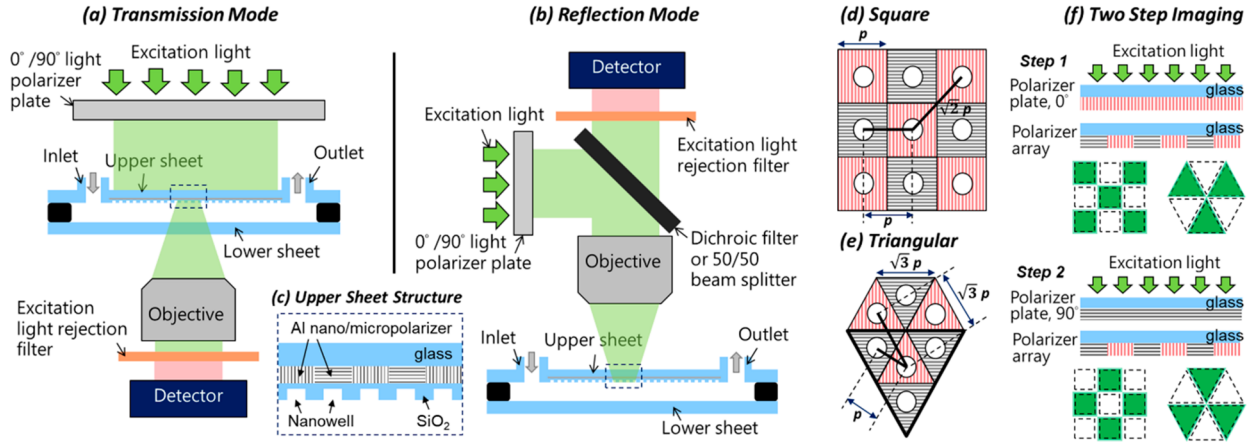

Figure 2. Schematic illustration of the optical system, biochip with a nano/micropolarizer array, and two-step imaging working principle. *Optical system:* (a) In transmission mode, the excitation light passes through an angle-switchable light polarizer plate and the nano/micropolarizer array to irradiate the nanowells. The fluorescence signals from the reaction sites are collected on the other side of the fluidic chip. (b) In reflection mode, the excitation light passes through an angle-switchable light polarizer plate, a dichroic mirror, an objective, and the nano/micropolarizer array to irradiate the nanowells. The fluorescence signals from the reaction sites are collected on the same side of the fluidic chip through the same objective by a photodetector. *Biochip:* (c) The upper sheet structure of the fluidic chip contains a nanowell array on an Al nano/micropolarizer array. The nanowell and nano/micropolarizer arrays are in a (d) square or (e) triangular arrangement made of two orthogonally oriented nano/micropolarizer units. The pitch sizes, p, include 0.6, 0.9, 1.2, 1.5, 3, and 6 μm. (f) *Two-step imaging:* For the first image, the light polarizer plate is in the 0° orientation, and only the nanowells on the 0° polarized nano/micropolarizer units can be exposed to the excitation light. For the second image, the light polarizer plate is in the 90° orientation, and then the other nanowells on the 90° polarized nano/micropolarizer units can be exposed to the excitation light and the fluorescence signals can be collected.

loading of at most one bead in a nanowell for easy signal analysis. Because of photoresist (PR) protection during the amine modification process, the plain surface outside the nanowells was not treated with the positively charged amine groups and retained the native oxide properties, including the hydrophilicity and negative charge, to repel the negatively charged fluorescent beads (Figure 1i–k).

Principle and Optical Setup. To achieve spatial resolution improvement, an angle-switchable polarizer plate was inserted into the path of the excitation light of a conventional optical microscope to generate polarized light with different polarization angles for illumination (Figure 2a,b). Moreover, the nanowells or reaction sites were placed on an interspaced nano/micropolarizer array with two orthogonally oriented polarization angles of 0 and 90° (Figures 1 and 2c). Because the 0° polarized excitation light can only pass through the 0° nano/micropolarizer units to excite the above fluorophores and block the other half of the fluorescent signals on the 90° nano/micropolarizer units, the adjusted optical train can achieve the switchable interspaced excitation of the nanowells for two-image capture, with each half of the reaction signals applied for either the transmission (Figure 2a) or reflection mode (Figure 2b).

To attain the first polarization angle (0°) array interspersed with the second polarization angle (90°) array, square (Figure 2d) and triangular (Figure 2e) geometric structures of the interspaced nano/micropolarizer array were designed and allocated under the nanowells with a minimum well pitch of p and used as a fluidic biochip. Hence, the polarizer array was established with a minimum pitch of $\sqrt{2}p$ and $\sqrt{3}p$ for the nano/micropolarizer units with the same polarization angle in the square and triangular arrangements, respectively.

The two-imaging step was performed by capturing the first image *via* 0° polarized excitation light for signal collection of the reaction responses in the nanowells on the 0° nano/micropolarizer and then the second image *via* 90° polarized excitation light for signal collection of those on the 90° nano/micropolarizer (Figure 2f). As a result, the original signal responses in the nanowells with a pitch size of p were theoretically captured by two images with a minimum pitch of $\sqrt{2}p$ and $\sqrt{3}p$ for the square and triangle shapes, respectively, to achieve resolution improvement.

Polarizer Optical Property. The basic criteria of the design for the nano/micropolarizer array and the light polarizer plate are that the extinction ratio should be sufficient so that the unwanted signals on the orthogonal nano/micropolarizer units can be fully depressed and act as background, and the transverse magnetic (TM) transmittance through the light polarizer plate and the nano/micropolarizers at the excitation and emission light wavelengths of the target fluorophores should be relatively high.

Since the fluorescent beads that we used to demonstrate a single bead in a nanowell on each nano/micropolarizer unit had excitation/emission wavelengths of 542/612 nm, the TM transmittance and extinction ratio based on different thicknesses, grating periods, and fill factors were simulated (Figure S1a–d). Finally, we fabricated the Al grating structures in three thicknesses of 135, 180, and 225 nm with a period of 300 nm and a designed fill factor of 0.5 to measure their optical performances and fabrication profiles (Figures S1e,f and S2). In Figure S1a,b, a thickness of 180 nm and a fill factor of 0.5 show the highest transmittance at 542 and 612 nm, and the smaller grating period achieves better transmittance. In Figure S1c,d, the transmittance and extinction ratio are highly dependent on the fill factor and thickness: a thicker fabricated polarizer plate achieves transmittance spectra with gentler slopes, a larger fill factor results in a greater red shift of the transmittance spectra and lower transmittance intensities, and both the larger fill factor and thickness values result in a larger extinction ratio.

For an ideal case, the Al nano/micropolarizer array should be fabricated with a thickness of 180 nm, a fill factor of 0.5, and

https://doi.org/10.1021/acsanm.1c01936
ACS Appl. Nano Mater. 2021, 4, 10409–10418

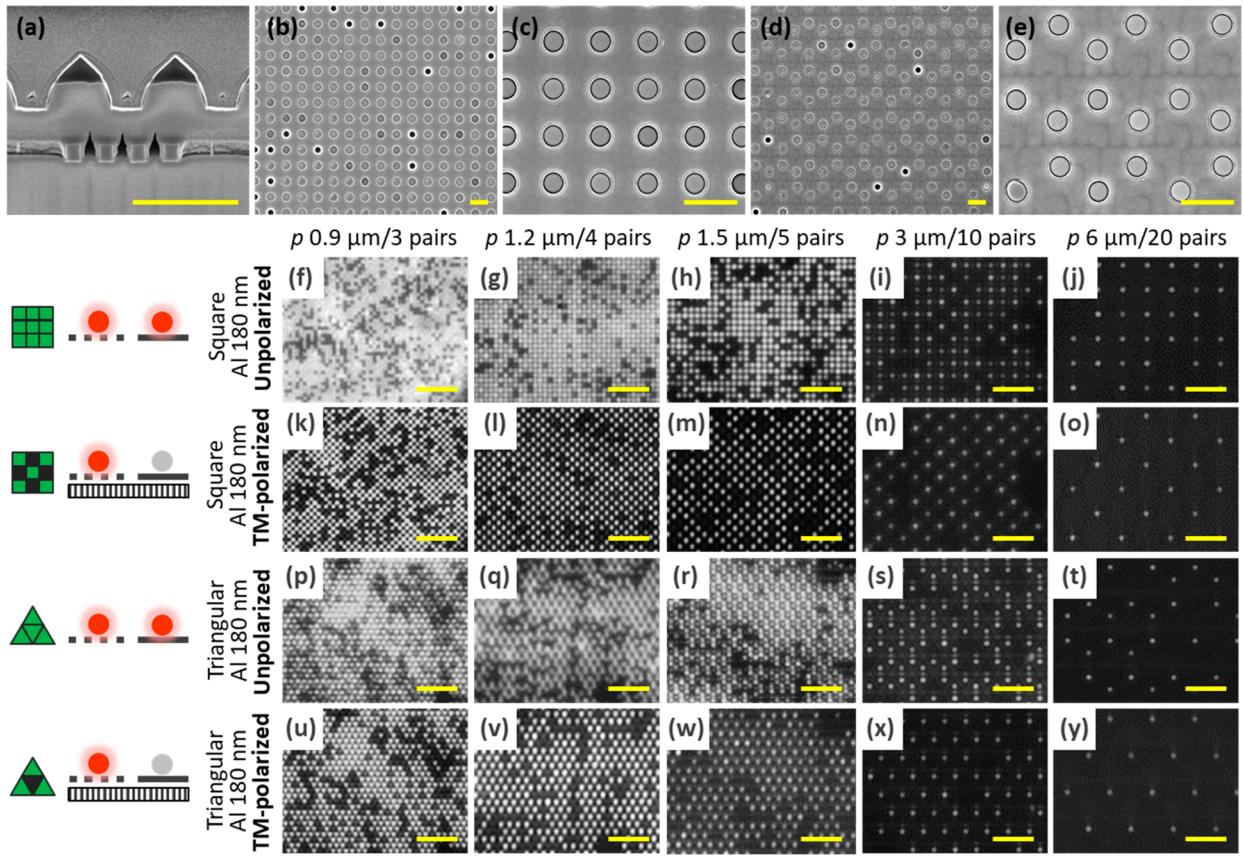

Figure 3. Nano/micropolarizer array biochip for fluorescent bead loading and imaging. (a) Cross-sectional SEM image of the square arrangement of the nano/micropolarizer array with a 180 nm Al thickness and a 0.9 μm pitch size before surface coating and PR removal. Top-view SEM images of the 0.9 μm pitch arrays in the (b, c) square arrangement and (d, e) triangular arrangement after bead loading. (f–y) Fluorescence images of bead-loaded nano/micropolarizer array chips obtained through the reflection mode instrumental setup: (f–j) square arrangements with unpolarized excitation light; (k–o) square arrangements with 0° TM polarized excitation light; (p–t) triangular arrangements with unpolarized excitation light; (u–y) triangular arrangements with 0° TM polarized excitation light of pitch sizes of 0.9, 1.2, 1.5, 3, and 6 μm, respectively. Scale bar: 1 μm in (a)–(e) and 10 μm in (f)–(y).

a period of 50–250 nm. According to the literature,[28] more pairs of grating nanostructures in a nano/micropolarizer unit will result in a higher transmittance and a better extinction ratio. However, the minimum achievable period was 300 nm due to the resolution limit of 248 nm DUV lithography and etching selectivity. In Figure S1e,f, the fabricated Al grating polarizer with a thickness of 180 nm and a fill factor of 0.55 shows the highest extinction ratio, and the simulation spectra agree with the experimental results; some mismatch might originate from the nonideal grating profiles (refer to Figures S2a–f and S3). The experimental excitation-light transmittance and extinction ratio results of the Al nano/micropolarizer array (the fabricated nanostructures in Figure S2g–r) irradiated by 0° polarized 530 nm light are shown in Figure S4. The dark units show that the 0° polarized 530 nm excitation light cannot pass through the nano/micropolarizer units with a 90° polarization angle. Using 0° polarized excitation light, bright units occur at the nano/micropolarizers with the same polarization angle (0°), and it implies that only the fluorophores above the 0° polarized array can be excited and used to collect the emission signals. Thus, it can be assumed that the greater intensity difference between the bright and dark units (or the higher the pixelated extinction ratio of the nano/micropolarizer) will achieve the higher signal-to-noise ratio (SNR).

Fluorescence Signals with Irradiation by Unpolarized and Polarized Light. Since the simulation and experimental results show that Al with a 180 nm thickness and a 0.55 fill factor has the highest extinction ratio in the pixelated nano/micropolarizer array (in Figure S4) and a large polarizer plate (in Figure S1e,f), only the 180 nm nano/micropolarizer samples were further integrated with a SiO_2 nanowell with top/bottom diameters of 428 nm/288 nm for single Ø 400 nm fluorescence bead loading. The cross-section view after nanowell integration (Figure 3a) and the top view after bead loading (Figure 3b–e) show that the nanowell is aligned (with <65 nm overlay shift) with the center of the pixelated nano/micropolarizer units and that the fluorescent beads only existed and were immobilized in the nanowells. For the square arrangement irradiated by unpolarized excitation light (Figure 3f–j), all the fluorescent signals were resolvable, except for the array with a pitch size of 0.9 μm. After the insertion of a 0° light polarizer plate between the excitation light and chip, the signals of the 90° nano/micropolarizer units were suppressed as background (Figure 3k–o). Therefore, the bright spots on the 0° polarization units on the 0.9 μm square array became clear and distinguishable. In addition, the minimum pitch between any two spots was originally in a vertical/horizontal direction and changed to a diagonal direction after the insertion of the light polarizer plate. Similar results were obtained for the triangular arrangement in Figure 3p–y, but

https://doi.org/10.1021/acsanm.1c01936
ACS Appl. Nano Mater. 2021, 4, 10409–10418

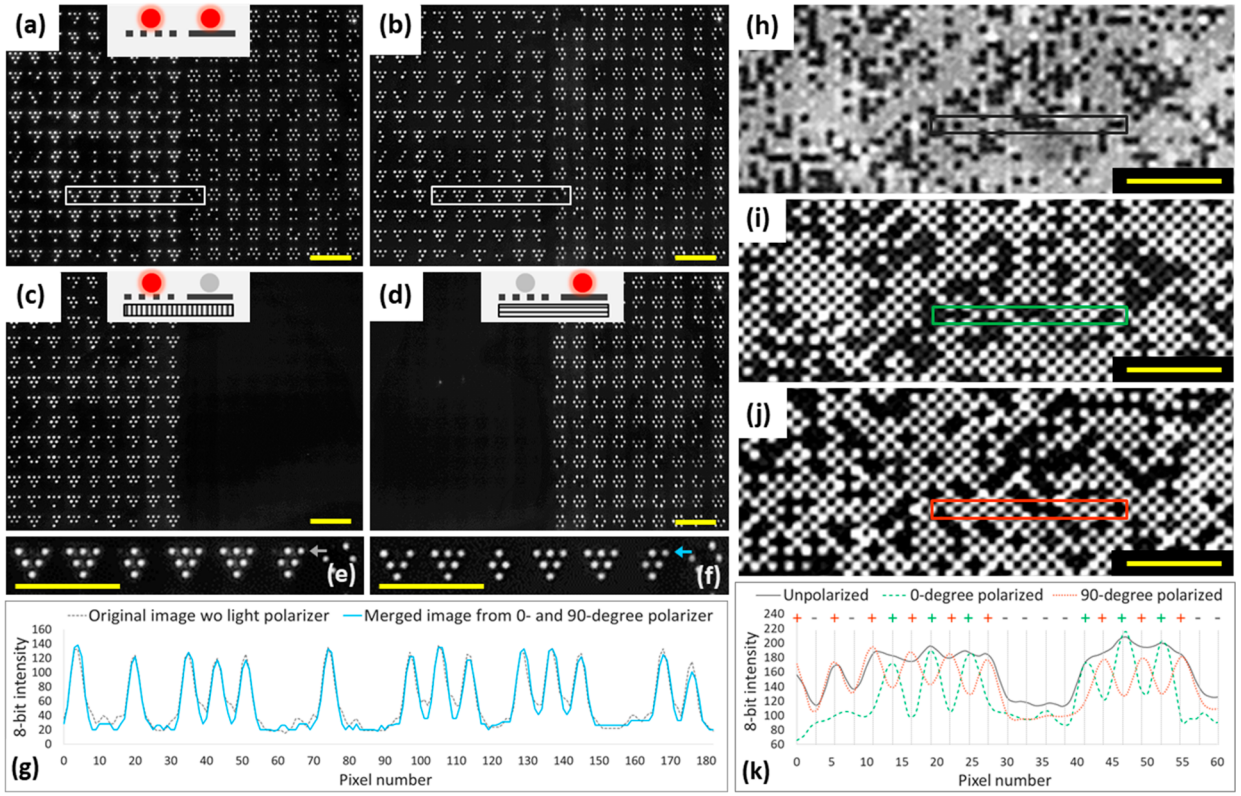

Figure 4. Two-polarization imaging and analysis. (a−d) Fluorescence images of a bead-loaded nano/micropolarizer array chip with a 180 nm Al thickness and a 1.5 μm triangular pitch size in reflection mode: (a) image excited by unpolarized excitation light with the 8-bit brightness adjusted by the lower/upper threshold of 20/200; (b) merged image from the image excited by 0° polarized excitation light and the image excited by 90° polarized excitation light, where the brightness is adjusted by the lower/upper threshold of 12/110; (c) image excited by 0° polarized excitation light; (d) image excited by 90° polarized excitation light. (e, f) Enlarged images of the white frames in (a) and (b), respectively. (g) Intensity profiles in the lateral direction indicated by the arrows in (e) and (f). (h−j) Fluorescence images of a bead-loaded nano/micropolarizer array chip with a 180 nm Al thickness and a 0.9 μm square pitch size in reflection mode: (h) image excited by unpolarized excitation light; (i) image excited by 0° polarized excitation; (j) image excited by 90° polarized excitation. (k) Intensity profiles in the lateral direction in the frame areas in (h−j). Scale bar: 20 μm in (a)−(f) and 10 μm in (h)−(j).

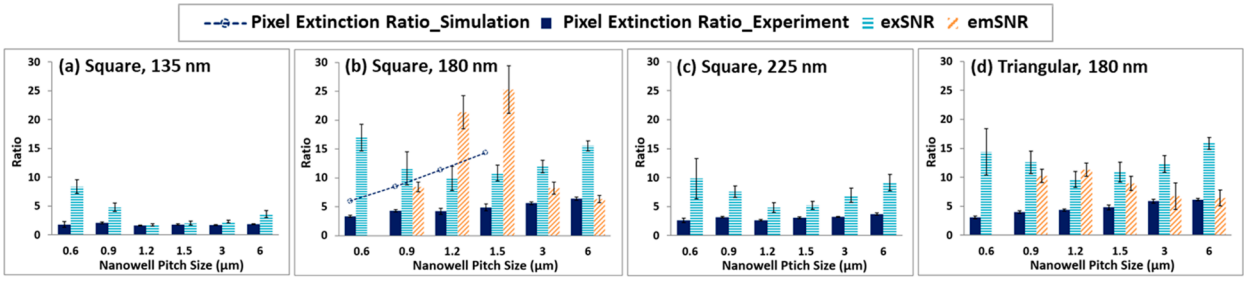

Figure 5. Experimental data of the excitation light pixelated extinction ratio, excitation light signal-to-noise ratio (exSNR), and fluorescent bead emission light signal-to-noise ratio (emSNR). Nano/micropolarizer arrays with a square arrangement and Al thicknesses of (a) 135, (b) 180, and (c) 225 nm. (d) Nano/micropolarizer array with a triangular arrangement and an Al thickness of 180 nm.

the asymmetric polarization directions of 0° (grating lines not parallel to any of the triangle side lengths) and 90° (grating lines in parallel to the bottom of the triangle side length) caused the intensity difference of the 0 and 90° units. After filtering of the weaker signals on the 90° nano/micropolarizer units *via* 0° polarized excitation, all pitch sizes can be resolved.

Two-Polarization Imaging and Analysis. For the comparison of imaging with and without a light polarizer plate, we designed a region with two different patterns: the left half was nanowells only placed on the nano/micropolarizer array with the 0° polarization angle and the right half was nanowells only on that with the 90° polarization angle. The fluorescence image excited by unpolarized light is shown in Figure 4a, with an 8-bit brightness adjustment with a threshold of 20−200, and the merged image from that excited by 0° polarized light and that excited by 90° polarized light is shown in Figure 4b, with an 8-bit brightness adjustment with a threshold of 12−110. The clean background in half of the images excited by either 0° (Figure 4c) or 90° (Figure 4d) polarized light provides evidence that the excitation light at a specified location could be completely prevented from generating fluorescence cross-talk among neighboring signals. The enlarged images (Figure 4e,f) and the intensity profiles (Figure 4g) show an obvious background suppression

https://doi.org/10.1021/acsanm.1c01936
ACS Appl. Nano Mater. 2021, 4, 10409−10418

Table 1. Pixelated Nano/micropolarizer Structure and Fluorescence Signal Property

(a) Length of Grating Nanostructures								
			0.6 μm	0.9 μm	1.2 μm	1.5 μm	3 μm	6 μm
square	vertical, V (nm)		377.4	686.0	988.3	1288.5	2787.7	5765.0
	horizontal, H (nm)		344.6	665.0	988.3	1279.9	2788.5	5795.0
	V/H ratio		1.0952	1.0315	1.0000	1.0067	0.9997	0.9948
triangle	vertical, V (nm)		726.2	1177.3	1638.6	2106.2	4314.7	8918.9
	horizontal, H (nm)		508.5	742.5	1130.5	1440.2	3340.5	7027.0
	V/H ratio		**1.4282**	**1.5856**	**1.4495**	**1.4625**	*1.2916*	*1.2692*
(b) Minimum Pitch and fwhm								
			0.6 μm	0.9 μm	1.2 μm	1.5 μm	3 μm	6 μm
square	pitch (μm)	no polarizer plate	N/A[a]	unresolvable	1.18	1.45	2.95	5.92
		0° polarizer plate	N/A	1.24	1.75	2.09	4.18	8.35
		90° polarizer plate	N/A	1.27	1.71	2.10	4.22	8.35
	fwhm (μm)	no polarizer plate	N/A	unresolvable	0.62 ± 0.09	0.82 ± 0.17	1.01 ± 0.12	1.17 ± 0.16
		0° polarizer plate	N/A	1.01 ± 0.11	0.90 ± 0.14	1.11 ± 0.17	1.15 ± 0.17	1.17 ± 0.20
		90° polarizer plate	N/A	1.00 ± 0.11	0.90 ± 0.14	1.18 ± 0.17	1.11 ± 0.17	1.17 ± 0.16
triangle	pitch (μm)	no polarizer plate	N/A	unresolvable	unresolvable	1.29	3.23	5.97
		0° polarizer plate	N/A	1.51	2.01	2.58	5.14	10.21
		90° polarizer plate	N/A	1.54	2.08	2.56	5.11	10.27
	fwhm (μm)	no polarizer plate	N/A	unresolvable	unresolvable	1.12 ± 0.23	1.01 ± 0.11	1.11 ± 0.17
		0° polarizer plate	N/A	0.81 ± 0.17	1.03 ± 0.13	0.95 ± 0.08	0.99 ± 0.08	1.13 ± 0.17
		90° polarizer plate	N/A	0.82 ± 0.17	0.98 ± 0.07	0.89 ± 0.14	0.94 ± 0.10	1.01 ± 0.11

[a]N/A, not available.

Table 2. Transmittance Difference Ratio and Signal Intensity

(a) Difference Ratio due to Leveling Angle Shift

			Leveling Angle Shift	0°	2.5°	5°	10°	15°	30°	45°
Simulation	Transmission	TM	@540 nm	0	-0.0058	-0.0243	-0.1170	-0.3748	-0.7015	-0.6914
			@610 nm	0	0.0003	0.0011	0.0031	0.0019	-0.2607	-0.6953
		TE	@540 nm	0	0.0004	0.0015	0.0080	0.0299	-0.1011	-0.3099
			@610 nm	0	-0.0007	-0.0027	-0.0106	-0.0231	-0.0635	-0.2570
	Log(TM/TE)		@540 nm	0	-0.0012	-0.0053	-0.0266	-0.1003	-0.2214	-0.1616
			@610 nm	0	0.0002	0.0007	0.0024	0.0044	-0.0414	-0.1561

(b) Difference Ratio due to Rotation Angle Shift

			Rotation Angle Shift	0°	2.5°	5°	10°	15°	30°	45°
Simulation	Transmission	TM	@540 nm	0	-0.0019	-0.0075	-0.0299	-0.0665	-0.2482	-0.4965
			@610 nm	0	-0.0019	-0.0076	-0.0301	-0.0668	-0.2492	-0.4983
		TE	@540 nm	0	0.2692	1.0749	4.2670	9.4793	35.3771	70.7541
			@610 nm	0	0.5735	2.2896	9.0886	20.1907	75.3527	150.7053
	Log(TM/TE)		@540 nm	0	-0.0485	-0.1487	-0.3411	-0.4876	-0.7822	-1.0000
			@610 nm	0	-0.0797	-0.2098	-0.4100	-0.5467	-0.8092	-1.0000

(c) Signal Intensity based on Rotation Angle Shift

			Rotation Angle Shift	0°	5°	10°	15°	20°	30°	45°
Experimental	Intensity (Square Arrangement)	0° well	0.9-μm	3±1	4±1	3±1	5±1	4±2	2±1	2±1
			1.2-μm	17±3	23±4	18±3	19±3	18±3	14±2	13±2
			1.5-μm	37±3	44±3	41±2	37±3	37±2	27±2	21±2
			3-μm	61±2	59±2	62±3	60±2	53±2	49±2	24±1
			6-μm	135±2	128±7	131±5	123±2	119±1	101±1	56±3
		90° well	0.9-μm	0±1	2±1	1±1	2±1	2±1	0±1	1±1
			1.2-μm	5±3	8±4	4±3	7±3	8±3	5±2	8±2
			1.5-μm	9±3	11±3	8±3	10±3	9±3	11±3	16±3
			3-μm	6±1	6±2	6±1	10±2	12±3	12±4	17±2
			6-μm	7±1	9±2	10±1	16±2	18±1	31±9	45±2

capability for the bright signals, although the intensity was weaker due to the transmission light loss *via* the light polarizer plate.

In Figure 4h–k, the 0.9 μm unresolvable fluorescence image in a square arrangement was recaptured *via* a 0° light polarizer plate and a 90° light polarizer plate to demonstrate the resolution improvement. According to the literature,[23,24] the

https://doi.org/10.1021/acsanm.1c01936
ACS Appl. Nano Mater. 2021, 4, 10409−10418

spatial resolution is ~854 nm (based on a 20×/NA0.5 objective, a camera pixel size of 6.45 μm, and a maximum wavelength of ~700 nm), which is in agreement with the unresolvable results obtained for the 0.9 μm square nanowell array. However, through this optical design and switching the polarization angle between 0 and 90°, a square array in an unresolvable pitch size could be read by two imaging captures with a $\sqrt{2}$-fold improved resolution.

Pixelated Extinction Ratio and SNR. For quantification, the pixelated extinction ratio, excitation light SNR (exSNR), and emission light SNR (emSNR) were calculated (as shown in Figure 5 based on Figure S5). Both the pixelated extinction ratio and exSNR show that the best performance occurs for the 180 nm thickness. The emSNRs obtained for the 180 nm nano/micropolarizer array ranges from 6.4 to 25.3, and 1.2 and 1.5 μm show notably higher emSNRs of 21.4 and 25.3 than their exSNRs of 9.9 and 10.9, respectively. This phenomenon may originate from the stronger excitation energy enhancement occurring for the nanowells with pixel sizes of 1.2 and 1.5 μm (refer to Figure S6).

Emission Signal Property of the Nano/micropolarizer Array. Table 1a summarizes the maximum lengths under the nanowells in the vertical direction for the 0° nano/micropolarizer units and the horizontal direction for the 90° nano/micropolarizer units. The V/H ratios in the triangular arrangement were ~1.5 and ~1.3 for the 0.6−1.5 μm and 3−6 μm pitch sizes, respectively, which were different from the ratio of ~1.0 for all pitch sizes of the square arrangement. This length of the 0° nano/micropolarizer unit was longer than that of the 90° nano/micropolarizer unit in the triangular arrangement, which is why the light transmittance intensity through the 0° nano/micropolarizer units is larger than the intensity through the 90° nano/micropolarizer units. The phenomenon of the nano/micropolarizer dimension being dependent on the intensity difference is also observed in Figure S7 and the literature,[42] which implies that the polarized excitation light intensity of this approach may need to be more than 5 times more intense to achieve a similar excitation energy on the fluorophores, and the additional emission intensity loss should be also considered for the reflection mode.

In super-resolution microscopy, the resolution improvement relies on the reduction in the PSF of fluorescence objects.[26,27] However, our approach only employs the polarization property to adjust the on/off excitation on the nanowells above the nano/micropolarizer array. In Table 1b, through the orthogonal-oriented polarization arrays with square and triangular arrangements, the minimum pitches increase by ~1.4 times and ~1.7 times, respectively. For the pitch sizes larger than 3 μm, the fwhm's are not obviously different, and the PSF was approximately 1.15 μm. For smaller pitch sizes, some measured fwhm's were smaller due to the effect of neighboring signal cross-talk.

Intensity Difference due to Leveling and Rotation Angles. Since the optical system consisted of one excitation light polarizer plate, the leveling and rotation angle tolerances were also simulated for their transmittance and extinction ratio (Figures S8 and S9). Table 2a,b summarizes the spectral difference ratio and indicates that the optical property is less sensitive to leveling angle shift than to rotation angle shift; therefore, the leveling angle shift can be ignored due to the sufficient alignment resolution of an optical-mechanical stage. For a rotation angle greater than 10°, the TE transmittance intensity rises on the two 90°-oriented polarizer plates, so it may be sensible to increase the background noise theoretically (refer to Figure S9d). The experimental results show a notable difference only when the rotation angle shift is larger than 15° (Table 2c and Figure S9e). For both leveling and rotation angle tolerances, angle shifts smaller than 10° can be acceptable.

EXPERIMENTAL METHODS

Materials. Red fluorescent 0.40 μm polystyrene beads (catalog no. R400, 1% solids, excitation/emission 542 nm/612 nm) were purchased from Thermo Scientific (USA). 3-Aminopropyltriethoxysilane (APTES; product no. 741442) and a Wash-N-Dry coverslip rack (product no. Z688568) were purchased from Sigma-Aldrich (USA). Eight-inch borosilicate glass (Schott BF33) with a thickness of 725 μm was purchased from WaferPlus Technology (Taiwan).

Optical System. A polarizer plastic sheet (product no. P50, 50 mm × 50 mm), as the light polarizer plate to generate polarized light from a monochromator for measuring the TM transmittance and extinction ratio of the fabricated polarizer plate, was purchased from 3Dlens Corp. (Taiwan). The monochromator (model MFS-630) was purchased from Hong-Ming Technology Co., Ltd. (Taiwan). The 530 nm high-intensity coaxial spotlight source (stock no. 11026), which worked with the light polarizer plate of the P50 polarizer plastic sheet to generate polarized 530 nm light in transmission mode (Figure 2a) for measurement of the pixelated extinction ratio and exSNR of the nano/micropolarizer array, and wire grid polarizer glass (stock no. 12647, 50 mm × 50 mm), which was equipped in an inverted microscope as the light polarizer plate in reflection mode (Figure 2b) for fluorescence imaging and calculation of emSNR, were purchased from Edmund Optics (USA). The microscope system CKX53 with an MPLN50X/NA0.75 objective for transmission mode and an UPLFLN20X/NA0.5 objective for reflection mode was purchased from Olympus (Japan). The Grasshopper3 USB3 camera (model no. GS3-U3-15S5C-C; 1.5 MP, 45 fps, SONY ICX825) was purchased from FLIR System, Inc. (USA).

Chip Fabrication Process. Each die includes two sections (Figure 1a): the bottom section is a 10 mm × 20 mm Al polarizer plate; the upper section includes the square and triangular structures of the nano/micropolarizer array with six nanowell pitch sizes, p, of 0.6, 0.9, 1.2, 1.5, 3, and 6 μm. An Al layer of 135, 180, or 225 nm was first deposited on the BF33 glass wafer (Figure 1b,c). As shown in Figure 1d,e, the grating structure with a 300 nm period was fabricated through DUV photolithography (FPA-5000 ES4 248 nm KrF Scanner, Canon, Japan) and two step etched by an AMAT DPSII etcher (DPSII Centura etcher, Applied Materials, USA). The first etching was performed under an RF power of 1200/50 W, a chamber temperature of 40 °C, a chamber pressure of 10 mTorr, a Cl_2/CHF_3 flow rate of 100/10 sccm, and an etching time of 60 s, and the second etching was performed under an RF power of 250/50 W, a $BCl_3/Cl_2/N_2/Ar$ flow rate of 20/40/10/60 sccm, and an etching time of ~54 s controlled by end-point detection. Followed by 700 nm SiO_2 deposition on the Al grating nano/micropolarizer, a 450 nm nanowell array was patterned through DUV photolithography with an alignment resolution of ~80 nm to the layer of the nano/micropolarizer array (Figure 1f,g). Etching was performed to remove SiO_2 to a thickness of ~350 nm by an AMAT DPSII etcher at an RF power of 500/85 W, a chamber temperature of 80 °C, a chamber pressure of 5 mTorr, a $BCl_3/Cl_2/Ar$ flow rate of 30/25/60 sccm, and an etching time of 345 s (Figure 1h).

Nanowell Treatment for Bead Loading. The PR retaining nanostructures were immersed in 1% APTES solution in 99.5% ethanol for 1 h to graft amine functional groups on the SiO_2 surface of the nanowells (Figure 1i). Next, the PR was removed by immersion of the chip in acetone and ethanol solution for 10 min each under ultrasonication. Then, the 1% 400 nm fluorescent beads were diluted 1:1 with 95% ethanol before being dropped onto the amine-modified chip (Figure 1j). An optional blow-dry process was performed to force the beads to load into the nanowells through the dragging force of

https://doi.org/10.1021/acsanm.1c01936
ACS Appl. Nano Mater. 2021, 4, 10409−10418

surface tension. After three bead loading cycles, the chip was ultrasonically cleaned in 95% ethanol for 10 min to remove excess fluorescent beads. Finally, the chip was rinsed in DI water and blown dry with air (Figure 1k).

Optical Property Simulation. The optical properties of the Al polarizer plate were simulated by GSolver software from Grating Solver Development Co. (USA), and the light intensity and distribution after the nano/micropolarizer array were simulated through the finite-difference time-domain (FDTD) method.

Extinction Ratio and SNR Calculation. The extinction ratio of the polarizer plate was the ratio of TM transmittance with the maximum transmitted intensity (through two parallel-oriented polarizer plates) to TE transmittance with the minimum intensity (through two orthogonally oriented polarizer plates) at different wavelengths. In Figure S5, the pixelated extinction ratio was defined as the ratio of the average intensity of S_1-S_5 (or S_1-S_3) to the average intensity of B_1-B_4 (or B_1-B_3) for the square arrangement (or triangular arrangement). The exSNR was calculated as the ratio of the average excitation light intensity of S_1-S_5 (or S_1-S_3) to the standard deviation of the background of B_1-B_4 (or B_1-B_3) for the square arrangement (or triangular arrangement). After bead loading and image capture *via* excitation/emission filters of 530−560 nm/580LP, the emSNR was calculated as the ratio of the average emission light intensity of S_1-S_4 (or S_1-S_3) to the standard deviation of the background region within the dashed line, representing the boundary of the outer pixels.

Length of Grating Measurement. The length of the nano/micropolarizer array was measured at the maximum lengths in the vertical direction for the 0° nano/micropolarizer unit and in the horizontal direction for the 90° nano/micropolarizer unit of the Al grating opening under the nanowell area.

Minimum Pitch and Full Width at Half-Maximum (fwhm). The minimum pitch was measured by averaging 10 peak-to-peak pixel distances between any of the two continuously bright dots, and the fwhm averaged the half-maximum widths from 10 continuous peaks without a light polarizer plate or with either 0 or 90° light polarizer plate (refer to Figure S10, 1.5 μm square nano/micropolarizer array as an example). Because the magnification is 20× and the pixel size of the camera is 6.45 μm, which means each camera pixel is 322.5 nm, the averaged pitch size and the fwhm can be obtained.

Signal Intensities at Rotation Shift. The chip was immersed in the 1:1 diluted bead loading solution and measured at the same parameters of imaging conditions for all pitch sizes.

CONCLUSIONS

This paper proposes a super-resolution approach to enable fluorescence-based DNA sequencing on a denser nanoarray. The insertion of a switchable light polarizer plate in a conventional fluorescence optical system and the integration of additional metal grating nanostructures on a transparent substrate are employed to generate interspaced excitation. Through two image captures, a $\sqrt{2}$-fold (or even $\sqrt{3}$-fold) improved resolution was demonstrated for a 0.9 μm nanowell pitch size, and this concept can be further applied for a denser nanowell array with a smaller pitch size (and/or a better optical performance) by the reduction of fabricated grating periods (and/or the increase of grating pairs) in one nano/micropolarizer unit. However, in addition to the doubling times of image captures, the excitation energy needs to be increased to at least 10-fold for the compensation of the light decay to half and 1/5 while passing through a light polarizer plate and a 0.9 μm nano/micropolarizer array, respectively.

ASSOCIATED CONTENT

Supporting Information

The Supporting Information is available free of charge at https://pubs.acs.org/doi/10.1021/acsanm.1c01936.

TM transmittance and extinction ratio of fabricated large polarizer plate; SEM image of fabricated large polarizer plate and nano/micropolarizer array; TM transmittance variation based on grating profile difference; TM transmittance image of nano/micropolarizer array *via* 0° polarized illumination; SNR calculation method; simulation of extinction ratio and excitation energy distribution of pixelated nano/micropolarizer array; transmittance intensity decay; leveling/rotation tolerance of two polarizing plates; calculation method of pitch size and fwhm (PDF)

AUTHOR INFORMATION

Corresponding Author

Hsin-Yi Hsieh − *VisEra Technologies Company Limited, Hsinchu City 30078, Taiwan;* orcid.org/0000-0002-2762-8856; Email: hy_hsieh@viseratech.com

Authors

Chung-Hao Lin − *VisEra Technologies Company Limited, Hsinchu City 30078, Taiwan*

Wei-Ko Wang − *VisEra Technologies Company Limited, Hsinchu City 30078, Taiwan*

Chin-Chuan Hsieh − *VisEra Technologies Company Limited, Hsinchu City 30078, Taiwan*

Complete contact information is available at: https://pubs.acs.org/10.1021/acsanm.1c01936

Author Contributions

H.-Y.H. conceived of the two-polarization imaging process for the orthogonally orientated nano/micropolarizer array biochip. H.-Y.H. and C.-C.H. discussed the design and performance of the experiments. H.-Y.H. analyzed the measurement data with the assistance of C.-H.L. and W.-K.W.'s simulation of the extinction ratio and the energy distribution of the excitation light passing through the nano/micropolarizer array. H.-Y.H. wrote the manuscript with input from all of the authors.

Notes

The authors declare no competing financial interest.

ACKNOWLEDGMENTS

The authors thank Nanoelectronic Laboratory, Electronic and Optoelectronic System Research Laboratories (EOSL) of the Industrial Technology Research Institute (ITRI) for the fabrication of the large polarizer plate and nanowell-integrated nano/micropolarizer array chip and Dr. Po-Chou Chen for the transmittance and extinction ratio simulation of the plate polarizer, including grating profile variation, rotation/leveling tolerance, fill factor variation, and thickness variation.

ABBREVIATIONS

APTES = 3-aminopropyltriethoxysilane
DUV = deep ultraviolet
emSNR = signal-to-noise ratio of emission light of a fluorophore through pixelated nano/micropolarizer array
exSNR = signal-to-noise ratio of excitation light passing through pixelated nano/micropolarizer array
FDTD = finite-difference time domain
MacEtch = metal-assisted chemical etching
NA = numerical aperture
NGS = next-generation sequencing
PALM = photoactivated localization microscopy

PR = photoresist
PSF = point spread function
SEM = scanning electron microscopy
SIM = structured illumination microscopy
SNR = signal-to-noise ratio
STED = stimulated emission depletion
STORM = stochastic optical reconstruction microscopy
TE = transverse electric
TM = transverse magnetic
WD = working distance

REFERENCES

(1) Hsieh, H.-Y.; Peng, Y.-H.; Lin, S.-F.; Chen, L.-C.; Yu, T.-C.; Chiou, C.-F.; Lee, J. Triple-Junction Optoelectronic Sensor with Nanophotonic Layer Integration for Single-Molecule Level Decoding. *ACS Nano* **2019**, *13*, 4486−4495.
(2) Sathish, S.; Ricoult, S. G.; Toda-Peters, K.; Shen, A. Q. Microcontact Printing with Aminosilanes: Creating Biomolecule Micro- and Nanoarrays for Multiplexed Microfluidic Bioassays. *Analyst* **2017**, *142*, 1772−1781.
(3) Takulapalli, B. R.; Morrison, M. E.; Gu, J.; Zhang, P. A Nanocontact Printing System for Sub-100 nm Aligned Patterning. *Nanotechnology* **2011**, *22*, 285302.
(4) Barcelo, S. J.; Kim, A.; Wu, W.; Li, Z. Fabrication of Deterministic Nanostructure Assemblies with Sub-nanometer Spacing Using a Nanoimprinting Transfer Technique. *ACS Nano* **2012**, *6*, 6446−6452.
(5) Valsecchi, C.; Gomez Armas, L. E.; Weber de Menezes, J. Large Area Nanohole Arrays for Sensing Fabricated by Interference Lithography. *Sensors* **2019**, *19*, 2182.
(6) Vala, M.; Homola, J. Multiple Beam Interference Lithography: A Tool for Rapid Fabrication of Plasmonic Arrays of Arbitrary Shaped Nanomotifs. *Opt. Express* **2016**, *24*, 15656−15665.
(7) Xu, X.; Yang, Q.; Wattanatorn, N.; Zhao, C.; Chiang, N.; Jonas, S. J.; Weiss, P. S. Multiple-Patterning Nanosphere Lithography for Fabricating Periodic Three-Dimensional Hierarchical Nanostructures. *ACS Nano* **2017**, *11*, 10384−10391.
(8) Hsieh, H.-Y.; Xiao, J.-L.; Lee, C.-H.; Huang, T.-W.; Yang, C.-S.; Wang, P.-C.; Tseng, F.-G. Au-Coated Polystyrene Nnanoparticles with High-Aspect-Ratio Nanocorrugations *via* Surface-Carboxylation-Shielded Anisotropic Etching for Significant SERS Signal Enhancement. *J. Phys. Chem. C* **2011**, *115*, 16258−16267.
(9) Huang, H.-C.; Kim, M.; Zhan, X.; Chabak, K.; Kim, J. D.; Kvit, A.; Liu, D.; Ma, Z.; Zuo, J.-M.; Li, X. High Aspect Ratio β-Ga_2O_3 Fin Arrays with Low-Interface Charge Density by Inverse Metal-Assisted Chemical Etching. *ACS Nano* **2019**, *13*, 8784−8792.
(10) Kim, J. D.; Kim, M.; Chan, C.; Draeger, N.; Coleman, J. J.; Li, X. CMOS-Compatible Catalyst for MacEtch: Titanium Nitride-Assisted Chemical Etching in Vapor Phase for High Aspect Ratio Silicon Nanostructures. *ACS Appl. Mater. Interfaces* **2019**, *11*, 27371−27377.
(11) Hsieh, H.-Y.; Wang, P.-C.; Wu, C.-L.; Huang, C.-W.; Chieng, C.-C.; Tseng, F.-G. Effective Enhancement of Fluorescence Detection Efficiency in Protein Microarray Assays: Application of a Highly Fluorinated Organosilane as the Blocking Agent on the Background Surface by a Facile Vapor-Phase Deposition Process. *Anal. Chem.* **2009**, *81*, 7908−7916.
(12) Gao, G.; Smith, D. I. Clinical Massively Parallel Sequencing. *Clin. Chem.* **2020**, *66*, 77−88.
(13) Hassibi, A.; Manickam, A.; Singh, R.; Bolouki, S.; Sinha, R.; Jirage, K. B.; McDermott, M. W.; Hassibi, B.; Vikalo, H.; Mazarei, G.; Pei, L.; Bousse, L.; Miller, M.; Heshami, M.; Savage, M. P.; Taylor, M. T.; Gamini, N.; Wood, N.; Mantina, P.; Grogan, P.; Kuimelis, P.; Savalia, P.; Conradson, S.; Li, Y.; Meyer, R. B.; Ku, E.; Ebert, J.; Pinsky, B. A.; Dolganov, G.; Van, T.; Johnson, K. A.; Naraghi-Arani, P.; Kuimelis, R. G.; Schoolnik, G. Multiplexed Identification, Quantification and Genotyping of Infectious Agents Using a Semiconductor Biochip. *Nat. Biotechnol.* **2018**, *36*, 738−745.
(14) Drmanac, R.; Sparks, A. B.; Callow, M. J.; Halpern, A. L.; Burns, N. L.; Kermani, B. G.; Carnevali, P.; Nazarenko, I.; Nilsen, G. B.; Yeung, G.; Dahl, F.; Fernandez, A.; Staker, B.; Pant, K. P.; Baccash, J.; Borcherding, A. P.; Brownley, A.; Cedeno, R.; Chen, L.; Chernikoff, D.; Cheung, A.; Chirita, R.; Curson, B.; Ebert, J. C.; Hacker, C. R.; Hartlage, R.; Hauser, B.; Huang, S.; Jiang, Y.; Karpinchyk, V.; Koenig, M.; Kong, C.; Landers, T.; Le, C.; Liu, J.; McBride, C. E.; Morenzoni, M.; Morey, R. E.; Mutch, K.; Perazich, H.; Perry, K.; Peters, B. A.; Peterson, J.; Pethiyagoda, C. L.; Pothuraju, K.; Richter, C.; Rosenbaum, A. M.; Roy, S.; Shafto, J.; Sharanhovich, U.; Shannon, K. W.; Sheppy, C. G.; Sun, M.; Thakuria, J. V.; Tran, A.; Vu, D.; Zaranek, A. W.; Wu, X.; Drmanac, S.; Oliphant, A. R.; Banyai, W. C.; Martin, B.; Ballinger, D. G.; Church, G. M.; Reid, C. A. Human Genome Sequencing Using Unchained Base Reads on Self-Assembling DNA Nanoarrays. *Science* **2010**, *327*, 78−81.
(15) Havlicek, J.; Dachsel, B.; Slickers, P.; Andres, S.; Beckert, P.; Feuerriegel, S.; Niemann, S.; Merker, M.; Labugger, I. Rapid Microarray-Based Detection of Rifampin, Isoniazid, and Fluoroquinolone Resistance in Mycobacterium Tuberculosis by Use of a Single Cartridge. *J. Clin. Microbiol.* **2018**, *56*, No. e01249-17.
(16) Barnard, S. M.; Bowen, M. S.; Bacigalupo, M. C. R.; George, W. N.; Brown, A. A.; Tsay, J. Gel Patterned Surfaces. US 9512422, Dec 6, 2016.
(17) Giani, A. M.; Gallo, G. R.; Gianfranceschi, L.; Formenti, G. Long Walk to Genomics: History and Current Approaches to Genome Sequencing and Assembly. *Comput. Struct. Biotechnol. J.* **2020**, *18*, 9−19.
(18) Reuter, J. A.; Spacek, D. V.; Snyder, M. P. High-Throughput Sequencing Technologies. *Mol. Cell* **2015**, *58*, 586−597.
(19) Shendure, J.; Balasubramanian, S.; Church, G. M.; Gilbert, W.; Rogers, J.; Schloss, J. A.; Waterston, R. H. DNA Sequencing at 40: Past, Present and Future. *Nature* **2017**, *550*, 345−353.
(20) *Next Generation Sequencing & DNA Synthesis: Technology, Consumables Manufacturing and Market Trends 2019*; Yole Developpement: April 2019.
(21) Pujals, S.; Feiner-Gracia, N.; Delcanale, P.; Voets, I.; Albertazzi, L. Super-Resolution Microscopy as a Powerful Tool to Study Complex Synthetic Materials. *Nat. Rev. Chem.* **2019**, *3*, 68−84.
(22) Sezgin, E. Super-Resolution Optical Microscopy for Studying Membrane Structure and Dynamics. *J. Phys.: Condens. Matter* **2017**, *29*, 273001.
(23) Vangindertael, J.; Camacho, R.; Sempels, W.; Mizuno, H.; Dedecker, P.; Janssen, K. P. F. An Introduction to Optical Super-Resolution Microscopy for the Adventurous Biologist. *Methods Appl. Fluoresc.* **2018**, *6*, 022003.
(24) Nieuwenhuizen, R. P. J.; Lidke, K. A.; Bates, M.; Puig, D. L.; Grünwald, D.; Stallinga, S.; Rieger, B. Measuring Image Resolution in Optical Nanoscopy. *Nat. Methods* **2013**, *10*, 557−562.
(25) Feiner-Gracia, N.; Pujals, S.; Delcanale, P.; Albertazzi, L. 15 - Advanced Optical Microscopy Techniques for the Investigation of Cell-Nanoparticle Interactions. In *Micro and Nano Technologies, Smart Nanoparticles for Biomedicine*; Ciofani, G., Ed.; Elsevier: 2018; pp 219−236.
(26) York, A. G.; Chandris, P.; Nogare, D. D.; Head, J.; Wawrzusin, P.; Fischer, R. S.; Chitnis, A.; Shroff, H. Instant Super-Resolution Imaging in Live Cells and Embryos *via* Analog Image Processing. *Nat. Methods* **2013**, *10*, 1122−1126.
(27) Müller, C. B.; Enderlein, J. Image Scanning Microscopy. *Phys. Rev. Lett.* **2010**, *104*, 198101.
(28) Li, P.; Kang, G.; Vartiainen, I.; Wang, F.; Liu, Y.; Tan, X. Investigation of Achromatic Micro Polarizer Array for Polarization Imaging in Visible-Infrared Band. *Optik* **2018**, *158*, 1427−1435.
(29) Tu, X.; Spires, O. J.; Tian, X.; Brock, N.; Liang, R.; Pau, S. Division of Amplitude RGB Full-Stokes Camera Using Micro-Polarizer Arrays. *Opt. Express* **2017**, *25*, 33160−33175.
(30) Vistnes, A. I. Reflection, Transmission and Polarization. In *Physics of Oscillations and Waves: With Use of Matlab and Python*; Undergraduate Texts in Physics; Springer: Cham, Switzerland, 2018; pp 293−334.

https://doi.org/10.1021/acsanm.1c01936
ACS Appl. Nano Mater. 2021, 4, 10409−10418

(31) Kong, N.; Tai, Y.-W.; Shin, S. Y. High-Quality Reflection Separation Using Polarized Images. *IEEE Trans. Image Process.* **2011**, *20*, 3393−3405.
(32) Sridhar, S.; Da Silva, A. Enhanced Contrast and Depth Resolution in Polarization Imaging Using Elliptically Polarized Light. *J. Biomed. Opt.* **2016**, *21*, 071107.
(33) Sun, D.; Huang, X.; Yang, K. A Multimodal Vision Sensor for Autonomous Driving. *Proceedings SPIE 11166, Counterterrorism, Crime Fighting, Forensics, and Surveillance Technologies III, Strasbourg, France*; SPIE: 2019; no. 111660L.
(34) Wu, F.; Zhao, B.-C.; Liu, Z.-S.; Lv, G.-J. Dual-View Integral Imaging Display Using a Polarizer. *Appl. Opt.* **2020**, *59*, 5785−5787.
(35) Zhang, H.; Deng, H.; He, M.; Li, D.; Wang, Q. Dual-View Integral Imaging 3D Display Based on Multiplexed Lens-Array Holographic Optical Element. *Appl. Sci.* **2019**, *9*, 3852.
(36) Ono, S. Snapshot Multispectral Imaging Using a Pixel-Wise Polarization Color Image Sensor. *Opt. Express* **2020**, *28*, 34536−34573.
(37) Pacheco, S.; Liang, R. Snapshot, Reconfigurable Multispectral and Multi-Polarization Telecentric Imaging System. *Opt. Express* **2014**, *22*, 16377−16385.
(38) Gao, X.; Wang, Q.; Cao, S.; Li, R.; Hong, R.; Zhang, D. Omnidirectional and Compact Transmissive Chromatic Polarizers Based on a Dielectric-Metal-Dielectric Structure. *Opt. Express* **2020**, *28*, 25073−25084.
(39) Lezec, H. J.; Degiron, A.; Devaux, E.; Linke, R. A.; Martin-Moreno, L.; Garcia-Vidal, F. J.; Ebbesen, T. W. Beaming Light from a Subwavelength Aperture. *Science* **2002**, *297*, 820−822.
(40) Keshavarz Hedayati, M.; Elbahri, M. Review of Metasurface Plasmonic Structural Color. *Plasmonics* **2017**, *12*, 1463−1479.
(41) Xu, T.; Wu, Y.-K.; Luo, X.; Guo, L. J. Plasmonic Nano-resonators for High-Resolution Colour Filtering and Spectral Imaging. *Nat. Commun.* **2010**, *1*, 59.
(42) Zeng, B.; Gao, Y.; Bartoli, F. J. Ultrathin Nanostructured Metals for Highly Transmissive Plasmonic Subtractive Color Filters. *Sci. Rep.* **2013**, *3*, 2840.
(43) Hsieh, H.-Y. Bio-Chip, Bio-Detection System and Bio-Detection Method. US App. 17/071736, Oct 15, 2020.

https://doi.org/10.1021/acsanm.1c01936
ACS Appl. Nano Mater. 2021, 4, 10409−10418